Editors' Suggestion

Ferrimagnetic spin waves in honeycomb and triangular layers of $Mn_3Si_2Te_6$

G. Sala [1], J. Y. Y. Lin [1], A. M. Samarakoon,[2,3] D. S. Parker [4], A. F. May [4], and M. B. Stone [2,*]

[1]*Spallation Neutron Source, Second Target Station, Oak Ridge National Laboratory, Oak Ridge, Tennessee 37831, USA*
[2]*Neutron Scattering Division, Oak Ridge National Laboratory, Oak Ridge, Tennessee 37831, USA*
[3]*Materials Science Division, Argonne National Laboratory, Lemont, Illinois 60439, USA*
[4]*Materials Science and Technology Division, Oak Ridge National Laboratory, Oak Ridge, Tennessee 37831, USA*

A detailed analysis of the ferrimagnetic ground state of $Mn_3Si_2Te_6$ has been performed using inelastic neutron scattering. Although the proposed valence of the nominal Mn^{2+} ions would have quenched orbital angular momentum, a significant exchange anisotropy exists in $Mn_3Si_2Te_6$. This apparent exchange anisotropy is a manifestation of a weak spin-orbit coupling in the layered material. We employ a detailed simulation of the spin-wave spectrum coupling traditional refinement of dispersion parameters to image analysis techniques, while including Monte Carlo simulations of the instrumental resolution to accurately identify the exchange couplings to the third nearest neighbor. An independent validation of our results is made by comparing our final Hamiltonian to heat capacity measurements.

I. INTRODUCTION

Research has accelerated examining quantum materials with quasi-two-dimensional magnetic interactions. Physical examples of such systems are generally crystallographically layered with significant exchange interactions within planes and weaker interplane exchange interactions. Van der Waals compounds, i.e., compounds held together by van der Waals bonds, with exchange interactions [1–3] are one subclass of these materials. Other materials in this diverse family include cuprate [4] and iron-based superconductors [5], quasi-two-dimensional Mott insulators [6,7], and intermetallic materials [8,9]. This has been largely driven by the now-realized prospect of building heterostructures from materials with complementary properties [10–12]. Within this context, two-dimensional (2D) and quasi-2D materials are of fundamental interest from a bulk perspective, because they often manifest strong in-plane interactions and weak interplane interactions. For instance, the compounds $FePS_3$, $CrSiTe_3$, $MnPS_3$, and CrI_3 have layers connected by van der Waals bonds and demonstrate bulk magnetic ordering with anisotropic interactions yielding anisotropic properties, suppressed 3D ordering temperatures, two-dimensional order, and persistent short-range correlations above T_C [13–16].

We have chosen to examine the layered, three-dimensional ferrimagnetic system $Mn_3Si_2Te_6$ to look for predicted anisotropic exchange terms in the spin Hamiltonian. The layered structure is similar to recently examined magnetic van der Waals compounds albeit in a 3D material. Understanding the nature of the anisotropic interactions and spin-orbit coupling in $Mn_3Si_2Te_6$ has implications for both frustrated 3D materials as well as 2D van der Waals compounds. $Mn_3Si_2Te_6$

was first described as a semiconducting ferrimagnetic material with the stoichiometry $MnSiTe_3$ [17]. This early work characterized the ordering temperature as $T_c = 82$ K, an antiferromagnetic Curie-Weiss temperature of $\Theta_{CW} = 75$ K, and a significant anisotropic magnetization between the a and c axes. The stoichiometry was later corrected and the crystal structure was refined to be trigonal (space group $P\bar{3}1c$, no. 163) with room-temperature lattice constants $a = 7.029(2)$ and $c = 14.255(3)$ Å [18]. Importantly, the crystal structure was shown to be three-dimensional, with Mn atoms filling octahedral voids so that there is not a Van der Waals gap in $Mn_3Si_2Te_6$. Figure 1 illustrates the crystal structure. The lattice consists of planes of Mn^{2+} ions ($S = 5/2$, $L = 0$) alternating with planes of Te and Si atoms along the c-axis as shown in Fig. 1(a) [17,18]. The Mn^{2+} sites are arranged in two types of layers which alternate along the c axis. One layer of Mn atoms (Mn1) has a honeycomb structure, shown as red spheres in Fig. 1, and the other layer of Mn atoms (Mn2) are arranged in a sparser triangular lattice, blue spheres in Fig. 1. Note that the Mn2 sites are not immediately aligned with the Mn2 sites in the neighboring layers. This results in the genesis of an ABACAB stacking pattern in the crystal structure [18].

Recently, a long-range magnetic ordered phase was characterized below $T_c \approx 78$ K. This phase consists of ferromagnetically aligned moments in the ab plane with an antiferromagnetic alignment of moments for neighboring spins along the c axis [19]. The difference in the number of Mn sites in the two layers leads to an overall bulk ferrimagnetic behavior of the system. First-principles calculations established a likely competition between antiferromagnetic exchange interactions up to the third nearest neighbor Mn-Mn bonds. These geometrically frustrated interactions are illustrated as J_1, J_2, and J_3 in Fig. 1(b), and the ferrimagnetic ground state results from a dominance of the longer range J_3 over J_2. Density functional theory (DFT) calculations also
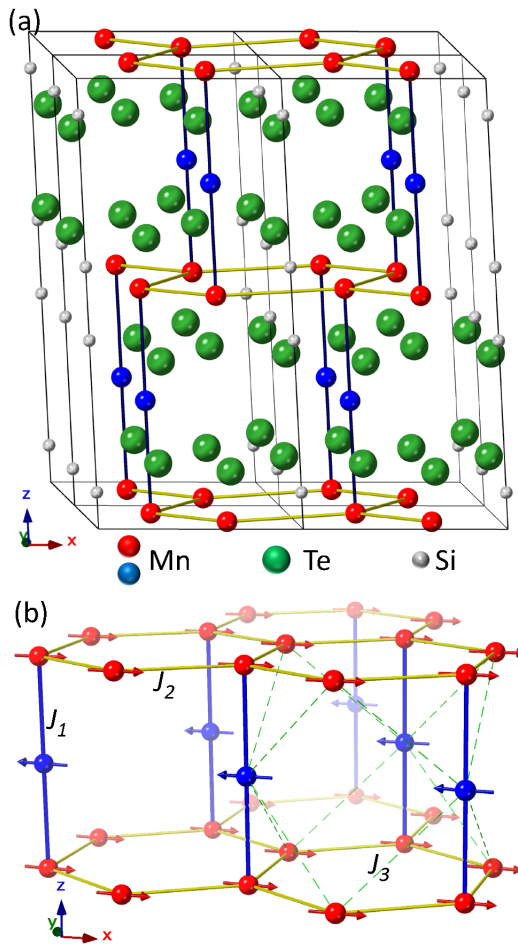
FIG. 1. (a) Crystal structure of the $Mn_3Si_2Te_6$ trigonal unit cell showing the layered arrangement of the Mn^{2+} ions and the location of the Te and Si sites [18]. The two nonequivalent Mn sites are illustrated with red (Mn1 on the $4f$ site) and blue (Mn2 on the $2c$ site) spheres. (b) Ordered magnetic structure of $Mn_3Si_2Te_6$ and proposed exchange couplings between magnetic sites. The arrows represent the easy-plane direction of the spins in the ordered phase. The exchange J_1 is shown as a blue line between Mn sites. The exchange J_2 is shown as a yellow line within the honeycomb layers of the Mn sites. The exchange J_3, dashed green lines, is only shown for one portion of the lattice for clarity of the figure.

proposed a finite amount of spin-orbit coupling to exist in the Hamiltonian, calling into question the nominal Mn^{2+} with a quenched orbital moment [19], the magnetism displays a large anisotropy on the order of 10 Tesla at $T = 5$ K, further suggesting the existence of this spin-orbit term in the relevant interactions in the magnetic Hamiltonian.

In the current study, we use inelastic neutron scattering to directly probe the spin-wave dispersion of $Mn_3Si_2Te_6$. We find that a Hamiltonian with anisotropic antiferromagnetic exchange is required to fully describe the resulting spectrum further validating the proposed spin-orbit interaction. The best model describes the dispersion, the heat capacity, and the magnetic density of states accurately, and it also confirms the ground-state spin orientation proposed in Ref. [19].

II. EXPERIMENTAL TECHNIQUES

$Mn_3Si_2Te_6$ was grown by chemical vapor transport (CVT) starting from the elements using iodine as a transport agent. The high-purity elements were sealed in a SiO_2 ampoule (Te Alfa Aesar 6N shot, Si Alfa Aesar 6N lump, Mn Alfa Aesar 99.98% granules). The ampoule was heated in a clam-shell furnace with a hot side kept at $800°$ C for 500 h. The starting materials were kept on the hot side and crystals grew throughout the entire ampoule; a gradient of approximately 40 deg over 15 cm existed. Sample orientation was first checked with x-ray diffraction off the as-grown facets and this verified a [001] normal orientation as expected. Magnetization measurements were utilized to further characterize the crystals and verify consistency with the previously reported melt-grown materials. The Curie temperature and anisotropy was observed to be consistent; however, the CVT grown crystals do not contain an anomaly near 300 K that has been observed in melt-grown crystals and is speculated to result from some type of intrinsic defect. This difference between CVT and melt-grown $Mn_3Si_2Te_6$ has been discussed in Refs. [19,20].

A single crystal sample was wrapped in aluminum foil and wired to a thin aluminum plate. Inelastic neutron scattering measurements were performed at the Spallation Neutron Source at the Oak Ridge National Laboratory using this crystal with the $(H0L)$ plane in the scattering plane of the instruments. Measurements at the SEQUOIA spectrometer were performed with $E_i = 60$ meV incident energy neutrons with the sample mounted to the cold finger of a bottom-loading closed-cycle refrigerator [21]. Measurements at the CNCS spectrometer were performed with $E_i = 12$ meV and the sample mounted to the sample stick of a liquid helium top-loading cryostat [22]. Both measurements were performed in high flux configurations of the instrument while rotating the sample about its vertical axis by at least 180 deg with a spacing of 1 deg to collect wave-vector dependent spectra throughout a volume of reciprocal space. The SEQUOIA/CNCS measurement was collected for 0.42/0.25 Coulombs of charge (≈5 min/≈3 min) on the spallation target for each value of rotation angle. Measurements were performed at two different instruments to obtain reasonable energy resolution across the entire band of magnetic excitations. Measurements were performed at $T = 5$ K and $T = 100$ K. Finally, the entire four-dimensional set of data was reduced, normalized, and properly symmetrized about the origin of the primary axes of the reciprocal lattice using the MANTID software package [23].

A. Background subtraction

The small sample size (≈90 micromoles of Mn, i.e., ≈49 mg) used in these measurements resulted in a relatively large background contribution from the scattering due to the sample mounting hardware and the sample environment itself. In order to analyze the spin wave dispersion in detail for such a small sample, the background needs to be adequately quantified. The first approximation of using the high-temperature, $T = 100$ K, measurement as a background for the low-temperature, $T = 5$ K, measurement was found to be problematic. Typically, above the ordering temperature, a band of magnetic scattering will often soften to lower
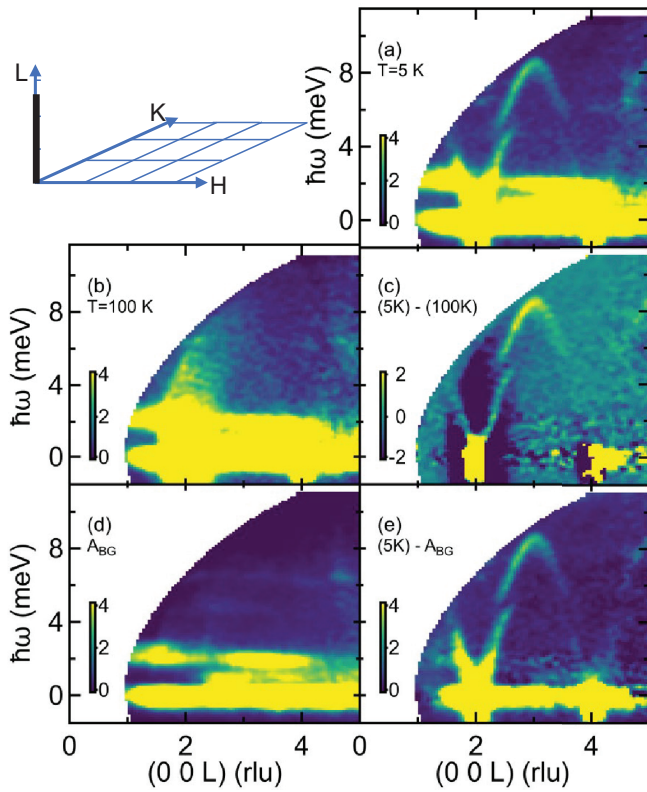
FIG. 2. Inelastic neutron scattering measurements of $Mn_3Si_2Te_6$ and background subtraction of these data. Each spectrum is shown on the same relative intensity with a color scale four units large. (a) $T = 5$ K measurement of the INS spectra for $Mn_3Si_2Te_6$ measured along the L-axis from the CNCS measurement. Data orthogonal to the wave-vector shown were integrated over a range of ± 0.1 reciprocal lattice units (rlu). (b) $T = 100$ K measurement of the INS spectra for $Mn_3Si_2Te_6$ measured along the L axis from the CNCS measurement. (c) Difference of the data shown in panels (a) and (b) with the high-temperature measurement subtracted from the low-temperature measurement. (d) Azimuthal determined background, A_{BG}, projected along the same direction as the data. (e) The difference between the $T = 5$ K measurement in panel (a) and the A_{BG} shown in panel (d). Inset in the upper left illustrates the path of the data through reciprocal space as a heavy black line

energy transfers and weaken in intensity. Concomitantly, the higher temperature measurement will enhance the scattering intensity of phonons which may overlap or pass through the magnetic spectrum. Thus, we found that both of these effects combined to produce a significantly oversubtracted low-temperature measurement when using the high-temperature data as a background. Figures 2(a) and 2(b) illustrates the $T = 5$ K and $T = 100$ K scattering intensity as a function of energy transfer, $\hbar\omega$, for wave vectors along the L axis in reciprocal lattice units (rlu). At $T = 5$ K, a dispersive magnetic mode can be seen emerging from the (002) wave vector. However, there is also significant scattering from the cryostat and/or sample mount for energies from 0 meV up to approximately 4 meV. The higher temperature measurement, Fig. 2(b) at $T = 100$ K, shows a broadening and softening of the magnetic mode to lower energy transfers and smaller values of wave-vector transfer. The difference of these two measurements,

shown in Fig. 2(c), is significantly oversubtracted near the $L = 2$ value. To avoid this, we use a heuristic approach similar to what has been done in Ref. [24] to quantify the background. For each incident energy, sample temperature measured and angular range, we generated a background data set based upon the detected neutrons within azimuthal sectors on the instrument detector which contributed to the lowest intensity for a given detector location and a small range of energy transfer [25]. The minimum scattering intensity for these sectors was chosen based upon the full range of rotation angles measured in each measurement. This azimuthally gleaned background, A_{BG}, is then traced back to its original neutron events and used to generate a separate file for background subtraction. This background is projected in reciprocal space in an identical manner as the original data, as shown in Fig. 2(d). The algorithm is able to quantify the significant background due to the powder scattering from the sample environment and sample mounting that is independent of the single crystal sample orientation. Figure 2(e) is the difference in the $T = 5$ K measurement and the A_{BG}. In this case, there is no significant oversubtraction, and the second minimum in the dispersion can now be seen at $L = 4$. Unless otherwise stated, we apply this type of gleaned background subtraction to our presented measurements.

III. EXPERIMENTAL RESULTS AND DISCUSSION

Figures 3(a)–3(d) shows the measured scattering intensity as a function of energy transfer, $\hbar\omega$, and wave-vector transfer along four particular directions within the reciprocal space of the crystal structure. Figure 4(a) shows the measured scattering intensity along the (H01) direction. We plot the lower energy transfer contours of the CNCS measurement on top of the SEQUOIA measurement to preserve reasonable energy resolution in different portions of the excitation spectrum. The measurements show two ranges of scattering intensity populated with excitations. There is a higher energy band of excitations between approximately 12 and 22 meV, and there is a lower band of gapless excitations between 0 and 8 meV. In each of these regions, there are at least two excitations that appear to cross one another. There is significant dispersion in the $(00L)$ direction and within the $(HK0)$ plane. However, there are also regions of reciprocal space that have flatter bands. The gap between the lower and higher energy modes indicates that there is likely an anisotropic exchange term in the Hamiltonian. Significant single-ion anisotropy is unlikely, given the lack of any gap in the spin-wave spectrum near zero energy transfer.

Figure 5 shows a series of constant wave-vector scans through the CNCS and SEQUOIA measurements. The solid and dotted lines in this figure are parametrizations of the scattering intensity using Gaussian line shapes with sloping backgrounds fit to the respective data. One can observe the presence of multiple modes and the dispersion in these modes as a function of wave-vector transfer. This procedure was extended to include 32 wave vectors throughout the measured volume of reciprocal space. These points were along the (0K1), (00L), (H00), (H01), (H02), (H03), and (H0H) wave vectors. Figures 3(e)–3(h) and 4(b) show the fitted peak
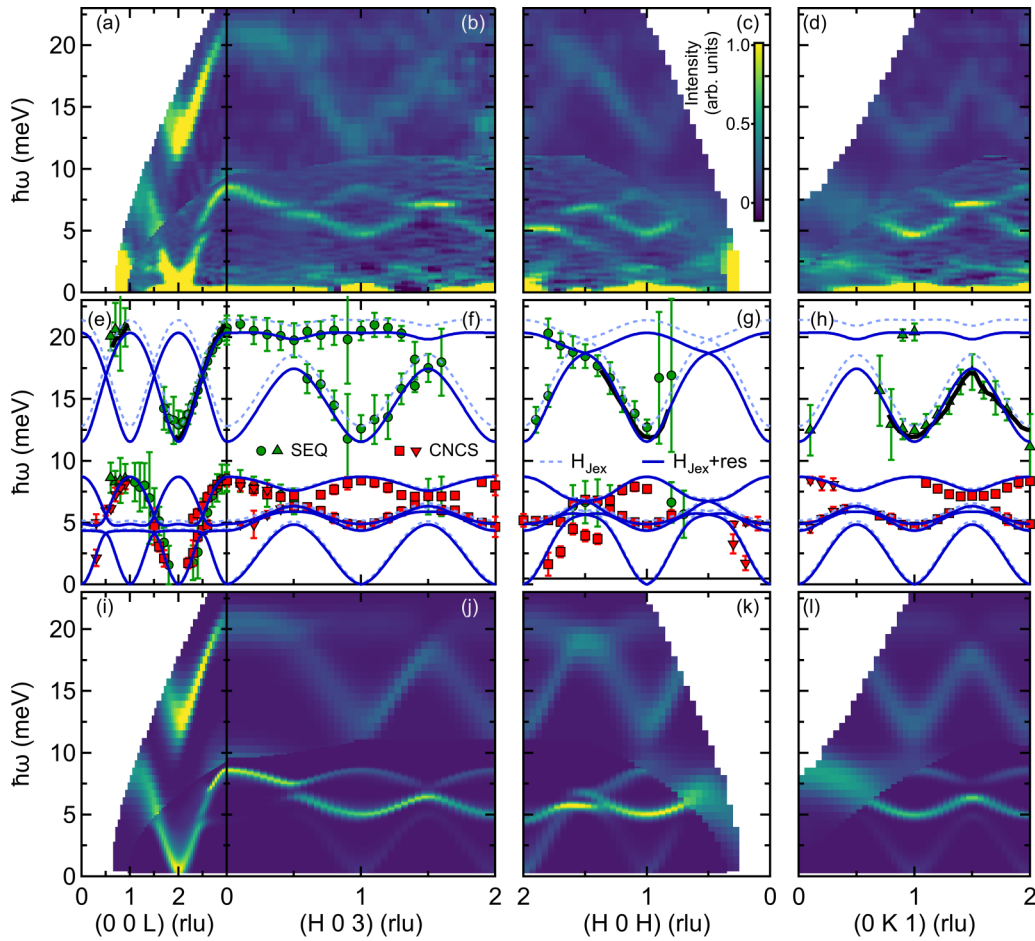
FIG. 3. Measured scattering intensity, determined spin-wave mode locations, calculated spin-wave dispersion, and calculated scattering intensity for $Mn_3Si_2Te_6$ at T=5 K. [(a)–(d)] $T = 5$ K measured INS intensity. The slices in reciprocal space shown to higher (lower) energy transfer are from the SEQUOIA (CNCS) measurement. Data have been background subtracted as described in the text. The scattering intensity from SEQUOIA has been multiplied by a factor of 20 to place it on the same intensity scale as the CNCS data. [(e)–(h)] Determined spin-wave mode energies as a function of energy transfer and wave-vector transfer. Green (red) points are from SEQUOIA (CNCS). Triangular symbols have energy values determined from higher Brillouin zones, but are shown at reduced wave vector to appear in the figure. Mode values were determined from Gaussian fits to constant wave-vector scans as described in the text and illustrated in Fig. 5. Error bars are the half width at half maximum (HWHM) of the determined Gaussian peak added in quadrature to the fitted error in peak location. Dashed blue lines are the calculated spin-wave mode energies based upon the exchange parameters listed in Table I for the H_{Jex} model using SPINW fits of only the dispersion. Heavy black lines correspond to resolution corrected dispersion based upon the image analysis described in the text. Solid blue lines are the calculated spin-wave mode energies based upon the exchange parameters listed in Table I for the H_{Jex} model using resolution-corrected mode energies. [(i)–(l)] Calculated scattering intensity from convolution of MCViNE-calculated resolution function for both the SEQUOIA and CNCS measurements based upon the model with the exchange parameters determined from the resolution-corrected dispersion analysis, $H_{Jex}^{res.}$, described in the text with the values listed in Table I. Data in panels (a)–(d) and (i)–(l) have been smoothed by a Gaussian smoothing algorithm.

TABLE I. Refined values of the exchange constants for $Mn_3Si_2Te_6$, for each model implemented in our refinement. The parameters determined from the resolution-corrected dispersion are shown for the Hamiltonian $H_{Jex}^{res.}$. The values of $\chi^2_{disp.}$ were determined from the SPINW software fitting the dispersion data. The values for χ^2 were determined through a comparison of the measured and calculated scattering intensity for the data shown in Figs. 3(a)–3(d) as described in the text [27].

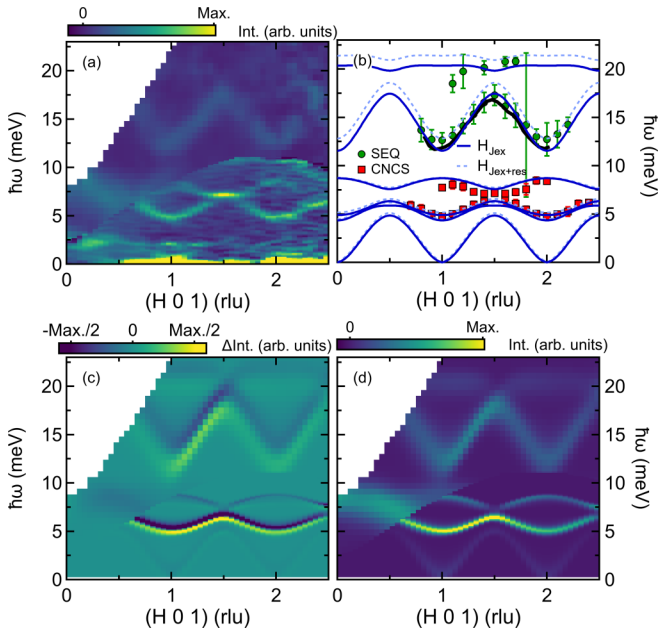| Hamiltonian	J_1 (meV)	J_2 (meV)	J_3 (meV)	D_H	D_T	Δ_1	Δ_2	Δ_3	$\chi^2_{disp.}$	χ^2
Heisenberg	1.398(3)	0.230(10)	0.718(10)						2.55	3.12
H_{XY}	1.400(6)	0.261(8)	0.776(9)	0.08(2)	0.08(2)				2.46	3.82
H_{Jex}	1.508(4)	0.457(4)	0.912(8)			1.140(9)	0.0138(7)	0.621(9)	1.74	3.31
$H_{Jex}^{res.}$	1.509(9)	0.449(3)	0.859(4)			1.171(6)	0.0271(8)	0.625(3)		2.24

FIG. 4. (a) $T = 5$ K measured INS intensity along (H01). Slice which extends to higher (lower) energy transfer is from the SEQUOIA (CNCS) measurement. Data have been background subtracted as described in the text. The scattering intensity from SEQUOIA has been multiplied by a factor of 10 to place it on the same intensity scale as the CNCS data. (b) Determined spin-wave mode energies as a function of energy and wave-vector transfer. Green (red) points are from the SEQUOIA (CNCS) measurement. Mode values were determined from Gaussian fits to constant wave-vector scans as described in text and illustrated in Fig. 5. Error bars are the half width at half maximum (HWHM) of the determined Gaussian peak added in quadrature to the fitted error in peak location. Dashed blue lines are the calculated spin-wave mode energies based upon the exchange parameters listed in Table I for the H_{Jex} model using SPINW fits of only the dispersion. Heavy black lines correspond to resolution-corrected dispersion based upon the image analysis described in the text. Solid blue lines are the calculated spin-wave mode energies based upon the exchange parameters listed in Table I for the H_{Jex} model using resolution-corrected mode energies. (c) Difference in calculated spin-wave scattering intensity between the determined dispersion using the H_{Jex} model and the resolution corrected H_{Jex} model in Table I. (d) Scattering intensity determined using the resolution corrected H_{Jex} model in Table I. Results in panels (a), (c), and (d) have been smoothed by a Gaussian smoothing algorithm.

locations and the determined mode energy from many of these fitted wave vectors (solid symbols).

Considering the classical magnetic moment on Mn^{2+} to be $S = 5/2$, and the spin-ordered magnetic structure, we use linear spin-wave (LSW) theory to calculate the magnetic excitations in order to determine the nature of the magnetic Hamiltonian. Prior first-principles calculations found that three competing antiferromagnetic Heisenberg exchange interactions, J_1, J_2, and J_3 as illustrated in Fig. 1, are able to account for the long-range ordered structure and the apparent suppression in the ordering temperature [19]. Note that a small spin-orbit coupling was previously considered to account for exchange anisotropies. Using the determined dispersion shown in Figs. 3(e)–3(h), we performed a refine-
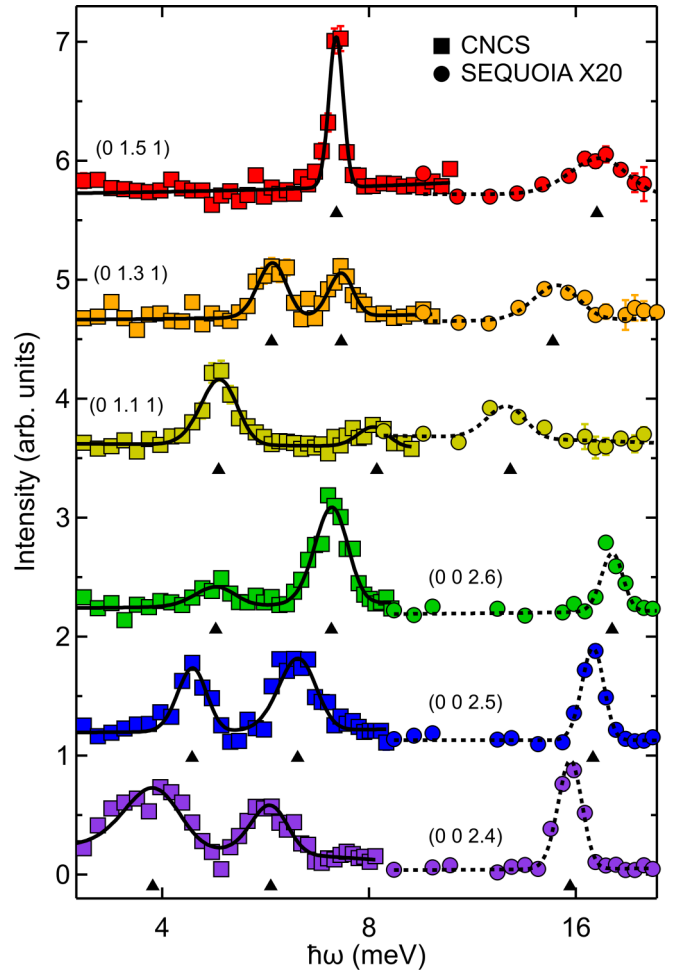
FIG. 5. Inelastic neutron scattering measurements of $Mn_3Si_2Te_6$ plotted as constant wave-vector scans from the $T = 5$ K CNCS (■) and SEQUOIA (●) measurements. Data have been offset along the vertical axis for presentation. The SEQUOIA measurements have been scaled by a factor of 20 to place them on the same intensity scale as the CNCS measurements. Solid (CNCS data) and dotted (SEQUOIA data) lines are comparisons of the measurement to either a single Gaussian with a sloping background or two Gaussians with a sloping background as described in the text. Data correspond to the wave vectors indicated in the figure. Data were integrated over the symmeterized slices shown in Figs. 3(a) and 3(d) without any smoothing over a range of ± 0.05 rlu. Black triangles are the fitted Gaussian peak locations for the respective modes they are beneath.

ment of the spin-wave dispersion using the SPINW software [26].

We first attempt to model the data using the Heisenberg Hamiltonian with the potential for only on-site anisotropies (i.e., single ion):

$$H_{XY} = J_1 \sum_{\langle i,j \rangle} \mathbf{S}_i \mathbf{S}_j + J_2 \sum_{\langle i,j \rangle} \mathbf{S}_i \mathbf{S}_j + J_3 \sum_{\langle i,j \rangle} \mathbf{S}_i \mathbf{S}_j$$
$$+ D_H \sum_h S_h^z S_h^z. + D_T \sum_t S_t^z S_t^z, \quad (1)$$

where the summation for the Heisenberg exchange is restricted to the relevant nearest neighbors, D_H and D_T

corresponding to the on-site anisotropy in the honeycomb and triangular lattice layers respectively, while the sums for the D terms are only for moments in the respective layers. A refinement of the pure Heisenberg model yields the terms $J_1 = 1.398(3)$, $J_2 = 0.230(10)$, and $J_3 = 0.718(10)$ meV. The pure Heisenberg model is not able to account for the gap in energies between mode branches [25]. Including on-site anisotropy yields similar values for the exchange terms $J_1 = 1.400(6)$, $J_2 = 0.261(8)$, $J_3 = 0.776(9)$, and small values of single-ion anisotropy, $D_H = 0.08(2)$ and $D_T = 0.08(2)$ meV. This model also is not able to account for the gap between the lower and upper bands of magnetic excitations between approximately 10 and 12 meV [25]. We quantify the resulting value by comparing the measured scattering intensity shown in Figs. 3(a)–3(d) to the resolution convolved scattering intensity for these directions using a single constant background and a multiplicative scale factor for the scattering intensity for each of the wave-vector directions shown. The chi-square value for this comparison of the dispersion points is $\chi^2 = 2.55$ and $\chi^2 = 2.46$ respectively as shown in Table I [27].

A Hamiltonian without on-site anisotropy, but which allows for anisotropic exchange interactions to account for the spin-orbit coupling previously described was also considered:

$$
\begin{aligned}
H_{\text{Jex}} = \; & J_1 \sum_{\langle i,j \rangle} \left[S_i^x S_j^x + S_i^y S_j^y + \Delta_1 S_i^z S_j^z \right] \\
& + J_2 \sum_{\langle i,j \rangle} \left[S_i^x S_j^x + S_i^y S_j^y + \Delta_2 S_i^z S_j^z \right] \\
& + J_3 \sum_{\langle i,j \rangle} \left[S_i^x S_j^x + S_i^y S_j^y + \Delta_3 S_i^z S_j^z \right],
\end{aligned}
\tag{2}
$$

where the summation is restricted to the relevant nearest neighbours. Allowing the values of Δ_1, Δ_2, and Δ_3 to independently vary improves substantially the comparison with the data and yields an improved refined dispersion with $J_1 = 1.508(4)$ meV, $J_2 = 0.457(4)$ meV, $J_3 = 0.912(8)$ meV, $\Delta_1 = 1.140(9)$, $\Delta_2 = 0.0138(7)$, and $\Delta_3 = 0.621(9)$ with $\chi^2 = 1.74$. Deviations from unitary values of Δ quantify the extent of spin-orbit interactions. The refined Δ terms indicate that the Mn1 sites are experiencing a greater influence of the spin-orbit interaction compared to the Mn2 sites. The dispersion is shown in Figs. 3(e)–3(h) and 4. Importantly, this improved refinement reproduces the gap between the high- and low-energy bands and therefore indicates that an apparent easy plane anisotropy is responsible for this feature in the spectrum. This anisotropy is a manifestation of the weak spin-orbit coupling in the compound [19].

A. Image analysis of dispersion

The refinement process just described, however, does not account for instrumental resolution effects which will often serve to sharpen or broaden dispersion relative to one another, or shift dispersions depending upon focusing effects across the spectrum. Here we describe an extension of an image analysis technique for the refinement of spin-wave dispersions that includes resolution effects. The energy resolution of the SEQUOIA measurement across the energy transfer range of 12 to 22 meV varies between 3.4 to 2.8 meV FWHM,

corresponding to a value of $\delta\hbar\omega/E_i = 5\%$ [28]. The energy resolution of the CNCS measurement between 0- and 10-meV energy transfer varies between 0.7 to 0.4 meV FWHM, corresponding to a value of $\delta\hbar\omega/E_i = 3$–6% for this range. We anticipate that resolution effects will be more significant in the determination of the dispersion from the SEQUOIA measurement.

From the first refined values of the Hamiltonian presented in Table I for Eq. (2), we can calculate the resolution convolved scattering intensities, where the resolution function is calculated from MCViNE [29,30] simulations using the dgsres package [31]. From this initial simulation, one can extract a series of constant wave-vector scans and refine peak locations of this calculated data using a Gaussian line shape, following the same procedure that was performed on the real experimental data. These extracted peak locations of the resolution-convolved model, $E_{\text{sim};0}(q)$, can be compared with the values of the dispersion determined at the respective wave vectors directly from the experimental data, $E_{\text{exp};0}(q)$. Their differences $\Delta E(q) = E_{\text{exp};0}(q) - E_{\text{sim};0}(q)$ can be used to correct the dispersion directly obtained from experimental data. However, such an approach is prone to unstable results for $\Delta E(q)$. Instead, a procedure inspired by the image disparity-map calculation technique was performed. This procedure solves the $\Delta E(q)$ curve by imposing a smoothness regularization [32]. The dispersion from the resolution-convolved data in the SEQUOIA measurement are systematically too high in energy transfer. This is a consequence of the three-dimensional dispersion surface and the steep dispersion in the vicinity of the antiferromagnetic zone centers convolved with the instrumental resolution of SEQUOIA operating in the high flux configuration. We determine the shifts in energy transfer, $\Delta E(q)$, for a series of wave vectors along the [00L], [H03], [H0H], [1K0], and [H01] directions for both the SEQUOIA and CNCS measurements. Regions of wave-vector transfer with good signal to noise ratios were chosen for this portion of the analysis to allow ultimately for direct comparison of the resolution convolved scattering intensity with the measured data. To first approximation, we correct for the resolution effects by applying the shifts $\Delta E(q)$ to the model dispersion directly obtained from experimental slices:

$$
E_{\text{exp};1}(q) = E_{\text{model};0}(q) + \Delta E(q). \tag{3}
$$

These shifted values of energy transfer are shown with the values originally determined via a Gaussian line-shape approximation in Figs. 3(e), 3(g) 3(h), and 4(b) as heavy solid lines. The spin-wave dispersion of the anisotropic Heisenberg exchange model, Eq. (2), can then be refined using the resolution function shifted peak locations, $E_{\text{exp};1}(q)$. This results in the exchange constants and anisotropy terms shown in Table I for the $H_{\text{Jex}}^{\text{res.}}$ model. Values of reduced chi square based upon a comparison of the measured and calculated scattering intensity for a subset of wave-vector transfers along the [00L], [H03], [H0H], and [1K0] directions can be calculated for the models examined and the resolution-corrected model. Originally, using the uncorrected values of the dispersion, the reduced chi-square value was 3.31, and this value decreased to 2.24 once the resolution correction was applied [27].
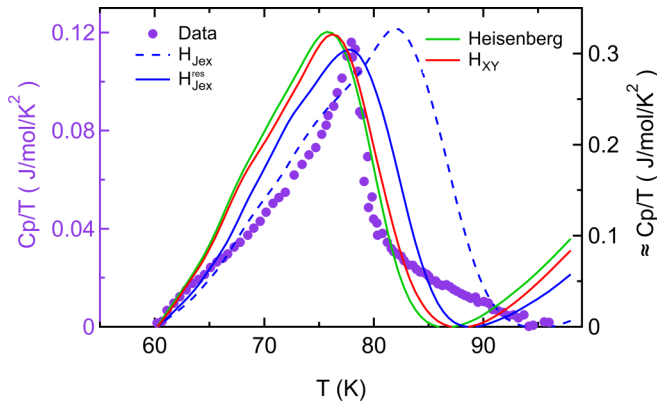
FIG. 6. Temperature normalized heat capacity as a function of temperature for $Mn_3Si_2Te_6$. Data are shown as purple circles plotted on the left axis. Lines (right axis) are the Monte Carlo calculation performed using Eq. (4) for the models tabulated in Table I.

The resulting refined dispersion curves for the resolution corrected model, $H_{Jex}^{res.}$ are shown in Figs. 3(e)–3(h) and 4(b). The refined and best exchange parameters are $J_1 = 1.509(9)$ meV, $J_2 = 0.449(3)$ meV, $J_3 = 0.859(4)$ meV, $\Delta_1 = 1.171(6)$, $\Delta_2 = 0.0271(8)$, and $\Delta_3 = 0.625(3)$. Figure 4(c) shows the change in scattering intensity of the calculated resolution convolved scattering intensity between the original and the resolution convolved H_{Jex} models. There are significant changes in the vicinity of the dispersive modes. One can also see the effects of the focused and defocused resolution condition on the SEQUOIA portion of the measurement. As visible, there is a greater shift in the calculated intensity in the vicinity of the local minima and maxima at the dispersion zone boundaries, while near flat regions of the dispersion are not significantly affected by the resolution effects. Figures 3(i)–3(l) and 4(d) are the calculated resolution-convolved scattering intensity for the anisotropic exchange model determined from the resolution corrected dispersion, $H_{Jex}^{res.}$. The comparison with the measured data is very good over wide ranges of energy and wave-vector transfer. We note that there are regions with lingering disparity between the measurement and the model. This includes data in the vicinity of 7-meV energy transfer and half-integer wave vectors as shown in Figs. 4(a) and 3(b)–3(d). The SEQUOIA measurements indicate that this region likely includes an optic or acoustic phonon that is contributing increasing scattering intensity at larger wave-vector transfer; see, for example, $[\frac{1}{2}03]$ and $[\frac{3}{2}03]$ in Fig. 3(b).

An independent validation of the determined Hamiltonian can be made by calculating thermodynamic quantities like heat capacity, which is a measurement of the energy fluctuations in the system. The heat capacity comparison shown in Fig. 6 is calculated via a standard Metropolis sampling algorithm by averaging over 96 independent sets of simulations on a $8 \times 8 \times 4$ supercell (1536 spins). The system has been slowly annealed from $T = 300$ K, down to $T = 50$ K, with 100 intermediate temperatures. At each temperature, the heat capacity is calculated by the total energy fluctuations [see Eq. (4)] over 10^6 Monte Carlo updates to ensure convergence, followed by a thermalization process with automatic

termination. Thus,

$$C_v = R \frac{\langle E^2 \rangle - \langle E \rangle^2}{T^2}, \tag{4}$$

where R is the gas constant and $\langle E \rangle$ represents the energy fluctuation of a spin configuration at fixed temperature T. We perform this calculation for the Heisenberg, H_{XY}, H_{Jex}, and $H_{Jex}^{res.}$ models in Table I. Finally, our Monte Carlo predicts the correct spin orientation in the ordered phase at $T = 0$ K, consistent with Ref. [19], further validating the proposed Hamiltonian. The peak location in the calculated heat capacity is found to agree very well with the $H_{Jex}^{res.}$ model's refined parameters.

IV. CONCLUSIONS

The magnetic Hamiltonian of $Mn_3Si_2Te_6$ was investigated by measuring its spin-wave dispersion at $T = 5$ K. The analysis of the data collected at SEQUOIA and CNCS confirmed the predictions on the spin orientation of this compound below its transition temperature with ferrimagnetic coupled spins. A neutron event-based azimuthal background subtraction was developed to improve the range of wave-vector and energy transfer over which the dispersion could be quantified. An efficient method of refining the terms in the Hamiltonian while accounting for resolution effects was also demonstrated. This allows one to refine the nature of the excitation spectrum including resolution effects without relying on the computationally intensive full numerical convolution of the resolution function with the model at every step of the model's refinement in a fitting algorithm.

The ratios of the determined exchange values, J_1, J_2, and J_3 shown in Table I agree reasonably well with the predictions in Ref. [19]. The underlying hexagonal layers in the crystal structure, the near crossing bands in the dispersion, and the presence of spin-orbit coupling suggests topological implications and the possibility of Dirac points in the dispersion. These points would occur where the spin-wave bands approach one another at similar locations in reciprocal space to such points in other compounds [33–35]. However, the Berry curvatures for these points in $Mn_3Si_2Te_6$ all have a value of zero, indicating that the near crossing points are not Dirac or Weyl points [36,37]. Nonetheless, our work establishes $Mn_3Si_2Te_6$ as a good example of a compound with a dispersion influenced by spin-orbit interactions and significant magnetic exchange orthogonal to a layered structure. It was found recently that one mechanism to tune the magnetization of $Mn_3Si_2Te_6$ is to use proton irradiation [38]. Our characterization of the energy scales present for the exchange interactions in $Mn_3Si_2Te_6$ may provide further understanding to the mechanism at play in the proton irradiation studies.

The U.S. Government retains and the publisher, by accepting the article for publication, acknowledges that the U.S. Government retains a nonexclusive, paid-up, irrevocable, worldwide license to publish or reproduce the published form of this manuscript, or allow others to do so, for U.S. Government purposes. The Department of Energy will provide public access to these results of federally sponsored research in accordance with the DOE Public Access Plan.

[1] S. Tian, J.-F. Zhang, C. Li, T. Ying, S. Li, X. Zhang, K. Liu, and H. Lei, J. Am. Chem. Soc. **141**, 5326 (2019).

[2] C. Gong, L. Li, Z. Li, H. Ji, A. Stern, Y. Xia, T. Cao, W. Bao, C. Want, Y. Wang, Z. Qiu, R. Cava, S. Louie, J. Xia, and X. Zhang, Nature (London) **546**, 265 (2017).

[3] B. Huang, G. Clark, E. Navarro-Moratalla, D. Klein, R. Cheng, K. Seyler, D. Zhong, E. Schmidgall, M. McGuire, D. Cobden, W. Yao, D. Xiao, P. Jarillo-Herrero, and X. Xu, Nature (London) **546**, 270 (2017).

[4] X. Shi, I. K. Dimitrov, T. Ozaki, G. Gu, and Q. Li, Phys. Rev. B **96**, 184519 (2017).

[5] P. Dai, Rev. Mod. Phys. **87**, 855 (2015).

[6] N. M. Hassan, K. Thirunavukkuarasu, Z. Lu, D. Smirnov, E. I. Zhilyaeva, S. Torunova, R. N. Lyubovskaya, and N. Drichko, Phys. Rev. B **104**, 245120 (2021).

[7] C. Wang, M.-Q. Tan, C.-M. Feng, Z.-F. Ma, S. Jiang, Z.-A. Xu, G.-H. Cao, K. Matsubayashi, and Y. Uwatoko, J. Am. Chem. Soc. **132**, 7069 (2010).

[8] B. C. Sales, J. Yan, W. R. Meier, A. D. Christianson, S. Okamoto, and M. A. McGuire, Phys. Rev. Materials **3**, 114203 (2019).

[9] S.-H. Do, K. Kaneko, R. Kajimoto, K. Kamazawa, M. B. Stone, J. Y. Y. Lin, S. Itoh, T. Masuda, G. D. Samolyuk, E. Dagotto, W. R. Meier, B. C. Sales, H. Miao, and A. D. Christianson, Phys. Rev. B **105**, L180403 (2022).

[10] Y. Liu, N. Weiss, X. Duan, H.-C. Cheng, Y. Huang, and X. Duan, Nat. Rev. Mater. **1**, 16042 (2016).

[11] D. Zhong, K. L. Seyler, X. Linpeng, R. Cheng, N. Sivadas, B. Huang, E. Schmidgall, T. Taniguchi, K. Watanabe, M. A. McGuire, W. Yao, D. Xiao, K.-M. C. Fu, and X. Xu, Sci. Adv. **3**, e1603113(2017).

[12] K. L. Seyler, D. Zhong, B. Huang, X. Linpeng, N. P. Wilson, T. Taniguchi, K. Watanabe, W. Yao, D. Xiao, M. A. McGuire, K.-M. C. Fu, and X. Xu, Nano Lett. **18**, 3823 (2018).

[13] D. Lançon, H. C. Walker, E. Ressouche, B. Ouladdiaf, K. C. Rule, G. J. McIntyre, T. J. Hicks, H. M. Rønnow, and A. R. Wildes, Phys. Rev. B **94**, 214407 (2016).

[14] T. J. Williams, A. A. Aczel, M. D. Lumsden, S. E. Nagler, M. B. Stone, J.-Q. Yan, and D. Mandrus, Phys. Rev. B **92**, 144404 (2015).

[15] S. Calder, A. V. Haglund, A. I. Kolesnikov, and D. Mandrus, Phys. Rev. B **103**, 024414 (2021).

[16] L. Chen, J.-H. Chung, T. Chen, C. Duan, A. Schneidewind, I. Radelytskyi, D. J. Voneshen, R. A. Ewings, M. B. Stone, A. I. Kolesnikov, B. Winn, S. Chi, R. A. Mole, D. H. Yu, B. Gao, and P. Dai, Phys. Rev. B **101**, 134418 (2020).

[17] R. Rimet, C. Schlenker, and H. Vincent, J. Magn. Magn. Mater. **25**, 7 (1981).

[18] H. Vincent, D. Leroux, D. Bijaoui, R. Rimet, and C. Schlenker, J. Solid State Chem. **63**, 349 (1986).

[19] A. F. May, Y. Liu, S. Calder, D. S. Parker, T. Pandey, E. Cakmak, H. Cao, J. Yan, and M. A. McGuire, Phys. Rev. B **95**, 174440 (2017).

[20] A. F. May, H. Cao, and S. Calder, J. Magn. Magn. Mater. **511**, 166936 (2020).

[21] G. E. Granroth, A. I. Kolesnikov, T. E. Sherline, J. P. Clancy, K. A. Ross, J. P. C. Ruff, B. D. Gaulin, and S. E. Nagler, J. Phys.: Conf. Ser. **251**, 012058 (2010).

[22] G. Ehlers, A. A. Podlesnyak, J. L. Niedziela, E. B. Iverson, and P. E. Sokol, Rev. Sci. Instrum. **82**, 085108 (2011).

[23] O. Arnold, J. Bilheux, J. Borreguero, A. Buts, S. Campbell, L. Chapon, M. Doucet, N. Draper, R. Ferraz Leal, M. Gigg, V. Lynch, A. Markvardsen, D. Mikkelson, R. Mikkelson, R. Miller, K. Palmen, P. Parker, G. Passos, T. Perring, P. Peterson *et al.*, Nucl. Instrum. Methods Phys. Res., Sect. A **764**, 156 (2014).

[24] J. C. Leiner, H. O. Jeschke, R. Valentí, S. Zhang, A. T. Savici, J. Y. Y. Lin, M. B. Stone, M. D. Lumsden, J. Hong, O. Delaire, W. Bao, and C. L. Broholm, Phys. Rev. X **9**, 011035 (2019).

[25] See Supplemental Material at http://link.aps.org/supplemental/10.1103/PhysRevB.105.214405 for further details regarding background subtraction and resolution analysis.

[26] S. Toth and B. Lake, J. Phys.: Condens. Matter **27**, 166002 (2015).

[27] We calculate χ^2 as $\chi^2 = \Sigma_i \frac{(O_i - E_i)^2}{E_i}$, where O_i is the observed intensity and E_i is the calculated intensity.

[28] D. L. Abernathy, J. L. Niedziela, and M. B. Stone, EPJ Web Conf. **83**, 03001 (2015).

[29] J. Y. Lin, H. L. Smith, G. E. Granroth, D. L. Abernathy, M. D. Lumsden, B. Winn, A. A. Aczel, M. Aivazis, and B. Fultz, Nucl. Instrum. Methods Phys. Res., Sect. A **810**, 86 (2016).

[30] J. Y. Lin, F. Islam, G. Sala, I. Lumsden, H. Smith, M. Doucet, M. B. Stone, D. L. Abernathy, G. Ehlers, J. F. Ankner *et al.*, J. Phys. Commun. **3**, 085005 (2019).

[31] dgsres: Neutron direct geometry spectrometer resolution calculators [https://doi.org/10.5281/zenodo.5137820]

[32] J. Y. Y. Lin, G. Sala, and M. B. Stone, Rev. Sci. Instrum. **93**, 025101 (2022).

[33] L. Chen, J.-H. Chung, M. B. Stone, A. I. Kolesnikov, B. Winn, V. O. Garlea, D. L. Abernathy, B. Gao, M. Augustin, E. J. G. Santos, and P. Dai, Phys. Rev. X **11**, 031047 (2021).

[34] B. Yuan, I. Khait, G.-J. Shu, F. C. Chou, M. B. Stone, J. P. Clancy, A. Paramekanti, and Y.-J. Kim, Phys. Rev. X **10**, 011062 (2020).

[35] A. Sapkota, L. Classen, M. B. Stone, A. T. Savici, V. O. Garlea, A. Wang, J. M. Tranquada, C. Petrovic, and I. A. Zaliznyak, Phys. Rev. B **101**, 041111(R) (2020).

[36] S.-S. Zhang, H. Ishizuka, H. Zhang, G. B. Halász, and C. D. Batista, Phys. Rev. B **101**, 024420 (2020).

[37] R. Matsumoto, R. Shindou, and S. Murakami, Phys. Rev. B **89**, 054420 (2014).

[38] L. M. Martinez, C. L. Saiz, A. Cosio, R. Omos, H. Iturriaga, L. Shao, and S. R. Singamaneni, MRS Adv. **4**, 2177 (2019).